Research Square

Preprints are preliminary reports that have not undergone peer review.
They should not be considered conclusive, used to inform clinical practice,
or referenced by the media as validated information.

Geophysics-informed groundwater mapping reveals slow-recovery zones after extreme drought

Zhengyang Fang
Central South University
Zhuo Liu
Central South University
Deshan Feng
Central South University
Yongfei Wang
Central South University
Rongwen Guo
Central South University
Hang Chen
hchen117@uiowa.edu

University of Iowa

Article

Keywords:

Posted Date: November 25th, 2026

DOI: https://doi.org/10.21203/rs.3.rs-11682015/v1

License: This work is licensed under a Creative Commons Attribution 4.0 International License.
Read Full License

Additional Declarations: No competing interests reported.

Geophysics-informed groundwater mapping reveals slow-recovery zones after extreme drought

Zhengyang Fang[1,2†], Zhuo Liu[1,3†], Deshan Feng[1], Yongfei Wang[1,4], Rongwen Guo[1*], Hang Chen[2*]

[1]School of Geosciences and Info-physics, Central South University, Changsha, 410083, China.
[2]School of Earth, Environment, and Sustainability, University of Iowa, Iowa City, IA, 52245, USA.
[3]Doerr School of Sustainability, Department of Earth and Planetary Sciences, Stanford University, Stanford, California, 94305, USA.
[4]Department of Mathematical Sciences, Tsinghua University, Beijing, 100084, China.

*Corresponding author(s). E-mail(s): rongwenguo@csu.edu.cn; hchen117@uiowa.edu;
†These authors contributed equally to this work.

Abstract

Groundwater buffers the impacts of extreme drought, but how subsurface heterogeneity shapes recovery within an aquifer remains poorly understood. We combined groundwater observations, airborne electromagnetic imaging, hydroclimatic forcing and pumping estimates in a graph-learning framework to reconstruct monthly water-table depth at 1-km resolution across the Mississippi River Valley alluvial aquifer from 2011 to 2023. The 2012 drought revealed three spatially distinct groundwater-response zones: Fast-recovery, Slow-recovery and Buffered zones. Slow early recovery was concentrated where thick, sand-rich deposits coincided with intensive irrigation pumping. By 2019, after several wetter years, 40% of Slow-recovery locations still had mean water levels below their pre-drought baseline. Pumping-reduction simulations showed that, for the same total reduction, an allocation guided by local water-table responses produced 13% greater regional storage gains than uniform reductions. However, most additional

storage accrued in areas with more advanced recovery, while locations with persistent deficits received smaller water-level improvements. These findings highlight the importance of subsurface heterogeneity for groundwater sustainability by linking aquifer architecture and groundwater use to post-drought recovery and conservation benefits. Accounting for this heterogeneity can help target pumping reductions to support both regional storage and recovery in persistently depleted areas.

Introduction

Extreme drought can rapidly deplete groundwater, especially in irrigated regions where pumping increases as rainfall and recharge decline [1–4]. The frequency and severity of such events are increasing under climate change [4], adding pressure to aquifers already stressed by long-term withdrawals [5–9]. Groundwater provides an important buffer during drought, but sustained drawdown can threaten water security and the long-term viability of irrigated agriculture [4,6,10–12]. Recovery does not necessarily follow the return of rainfall [12–15]. Water levels can respond to changing climate conditions over months to years [12,14,15], leaving groundwater deficits that persist through subsequent wet periods. How these deficits evolve after an extreme drought, and why recovery differs across an aquifer, remain important questions for groundwater management.

This uneven recovery also complicates decisions about how groundwater should be managed after drought [16,17]. Pumping restrictions, managed recharge and substitution with surface water have helped reverse groundwater declines in several heavily depleted aquifers [18–22]. Yet recovery within an aquifer need not occur uniformly: some areas may return to pre-drought water levels within a season, while others remain depleted for years despite experiencing the same sequence of wetter conditions [16,17,20]. A regional increase in groundwater storage can therefore coexist with persistent deficits in some locations. For management, this means that the amount of groundwater retained and where recovery occurs are distinct outcomes. This raises a

practical question for post-drought management: will the spatial allocation of pumping reductions that produce the largest storage gain also advance recovery in the places where drought deficits persist?

Answering this question requires understanding what controls groundwater response across an aquifer. Sediment properties, aquifer thickness and hydraulic connections influence how water levels respond to recharge and pumping [12,15,23–26], while the intensity and timing of groundwater withdrawals determine the stress imposed on the system [2,3,6,11,27]. Groundwater-level records show that wells within the same aquifer can follow markedly different drought trajectories under different hydrogeological conditions [16,17]. In heavily irrigated alluvial aquifers, these controls are closely linked: thick, permeable sand-rich deposits can support high groundwater yields as well as intensive withdrawals, linking aquifer productivity to the demands placed on it [25,28–30]. The recovery observed at any location therefore reflects the combined effects of aquifer architecture, climate and water use. These same factors also influence the response to reduced pumping, making it difficult to infer from historical recovery alone where a given pumping reduction would produce the greatest hydrologic benefit.

Resolving these responses requires groundwater histories and subsurface information at comparable spatial scales. Monitoring wells provide detailed records of water-level change through time, but their uneven distribution limits our ability to map recovery across an aquifer [20,31]. Satellite gravimetry captures broad changes in water storage, but at a resolution too coarse to distinguish responses among individual management areas [20,32,33]. Geophysical observations provide a different view by imaging the subsurface properties that influence groundwater storage and movement [34]. Airborne electromagnetic (AEM) surveys are particularly useful for regional aquifer characterization because they map variations in subsurface structure across

large areas [23,35–40]. In the lower Mississippi Valley, AEM surveys and borehole-constrained models have revealed regional sedimentary architecture and connectivity [23,24,41,42], with locally calibrated relationships between electrical resistivity and hydraulic properties [25]. Combining this spatial information with groundwater observations and time-varying hydrologic forcing provides a way to reconstruct drought recovery at scales relevant to groundwater management.

We test two related hypotheses in the Mississippi River Valley alluvial aquifer (MRVA), a heavily irrigated system [28–30,43] that experienced substantial groundwater decline during the 2012 extreme drought. First, we hypothesize that post-drought recovery is spatially organized by aquifer architecture and groundwater use. Second, we hypothesize that these spatial differences also shape the benefits of reduced pumping, making management outcomes sensitive to where pumping reductions are applied. The MRVA provides a suitable setting for these tests because regional AEM coverage overlaps a groundwater-monitoring network spanning the drought and subsequent recovery. We integrate groundwater observations, AEM resistivity, hydroclimatic forcing and pumping estimates in a geophysics-informed graph-learning framework to reconstruct monthly water-table depth at 1-km resolution from 2011 to 2023. We use the reconstructed record to identify recovery zones and relate them to subsurface architecture and pumping, and then conduct pumping-reduction experiments that hold the total conserved volume constant while varying its spatial allocation. These experiments test whether strategies that produce larger regional storage also advance recovery where drought deficits persist.

Results

Geophysics-informed reconstruction of groundwater change across the MRVA

We reconstructed monthly water-table depth (WTD) across 87,871 1-km grid cells in the MRVA from January 2011 to December 2023 by combining groundwater observations with infiltration, pumping, terrain and AEM resistivity (Fig. 1). The AEM data resolved broad three-dimensional differences in aquifer structure, including resistive, sand-rich alluvial deposits of variable thickness and more conductive intervals associated with finer-grained sediments [23–25] (Fig. 1d). These subsurface contrasts provided spatial information between monitoring wells, where direct groundwater observations were limited.

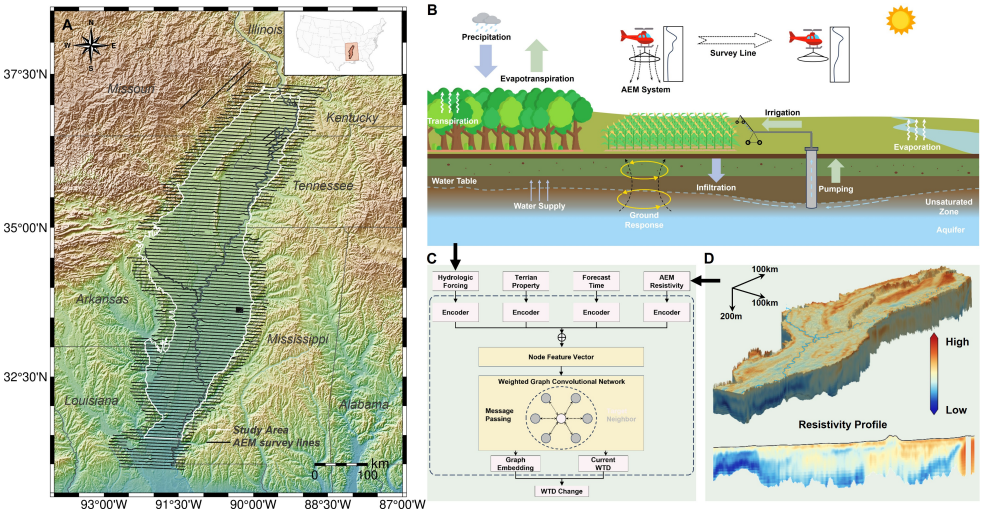

Fig. 1 Geophysics-informed reconstruction of groundwater change across the MRVA. a, Study region showing the MRVA, regional hydrographic context and AEM survey coverage. b, Conceptual representation of the precipitation, evapotranspiration, infiltration, pumping, irrigation and groundwater processes included in the reconstruction. c, Graph-learning workflow used to predict WTD change from infiltration, pumping, terrain properties, time encoding and AEM resistivity structure. d, Representative AEM resistivity volume and profile, illustrating the subsurface heterogeneity used as a geophysical constraint.

The reconstructed groundwater changes were consistent with observations withheld in both time and space (Supplementary Figs. S4 and S5; Table S1). The groundwater-storage anomaly derived from reconstructed WTD closely followed GRACE terrestrial-water-storage variability over the study period ($r = 0.91$; Fig. 2g). Positive correlations were also found across the four MRVA subregions (Supplementary Fig. S9). These comparisons show that the reconstruction captured the main seasonal and multi-year groundwater changes while retaining the spatial differences needed to compare drought decline and recovery across the aquifer.

The extreme drought reveals contrasting groundwater recovery zones

The 2012 drought provided a common stress event for comparing groundwater responses across the MRVA. Reduced precipitation and net infiltration coincided with strong growing-season pumping, followed by several wetter years that allowed recovery to be tracked over multiple years (Fig. 2g). We described each groundwater response using five metrics: maximum decline, decline rate, early recovery ratio, half-recovery time and long-term recovery ratio (Fig. 2a–e; Supplementary Fig. S13). These quantities showed different spatial patterns. Locations with large water-table declines did not necessarily recover slowly, and locations with similar drought-season declines could follow very different recovery paths. Therefore, the size of the initial decline did not by itself describe how groundwater recovered after the drought.

The five metrics separated the aquifer into Fast-recovery, Slow-recovery and Buffered zones (Fig. 2f). Fast-recovery zones covered 37.8% of the classified area and experienced the largest median decline, 2.02 m, but reached half-recovery in a median of only 3 months. Slow-recovery zones covered 35.2% of the area. Their median decline was smaller, 1.35 m, but the median early recovery ratio was 0.51 and the median half-recovery time was 8 months. Buffered zones covered the remaining 27.0% and

showed the weakest drought response, with a median maximum decline of 1.04 m and a median decline rate of 0.165 m/month. Differences among the zones remained evident over much longer timescales. By 2019, after several wetter years, 40.6% of locations in the Slow-recovery zone still had mean water levels below their 2011 mean water level. The spatial pattern of the three zones was also stable to perturbations of the reconstructed WTD field, with the dominant perturbed assignment matching the original zone at 82.4% of classified locations (Supplementary Fig. S15). These results show that groundwater decline and recovery were spatially distinct responses to the same drought, raising the question of why recovery remained slow in some parts of the aquifer.

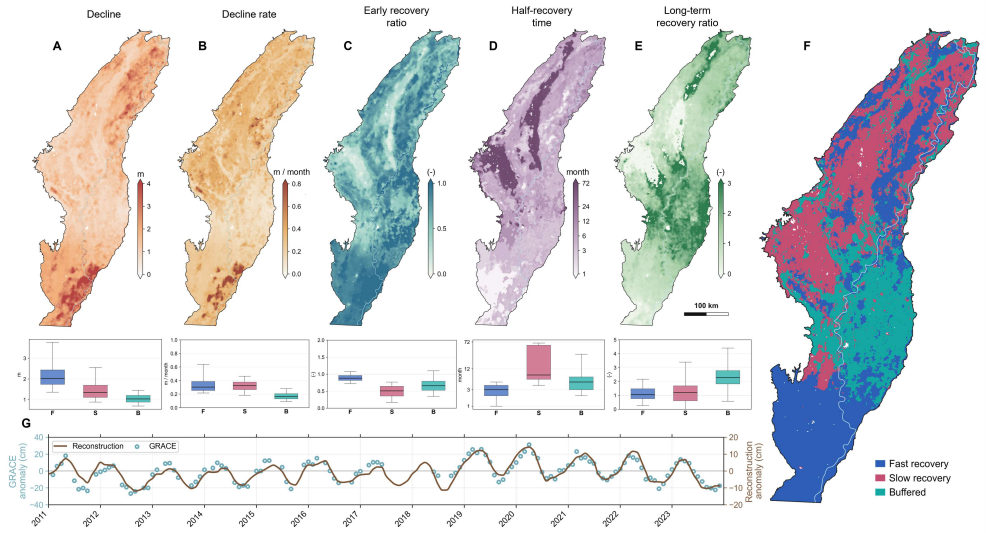

Fig. 2 Extreme drought reveals contrasting groundwater-recovery zones across the MRVA. a–e, Spatial distributions of maximum decline, decline rate, early recovery ratio, half-recovery time and long-term recovery ratio derived from the reconstructed response to the 2012 drought. Box plots summarize the distributions of each metric across Fast-recovery, Slow-recovery and Buffered zones. **f**, Spatial classification of the three groundwater-response zones based on the five drought-response metrics. **g**, Regional groundwater anomaly from the reconstruction compared with GRACE terrestrial-water-storage anomalies over the study period.

Subsurface architecture and pumping organize slow recovery

The three recovery zones differed systematically in both aquifer structure and groundwater use (Fig. 3; Supplementary Figs. S16–S19). Slow-recovery zones contained a thicker resistive interval than the other two zones. Median high-resistivity thickness was 46 m in Slow-recovery zones, compared with 21 m in Fast-recovery zones and 27 m in Buffered zones. Pumping showed the same broad contrast. Median May–October 2012 pumping was approximately 151,000 m^3 per cell in Slow-recovery zones, compared with 95,000 m^3 in Fast-recovery zones and 112,000 m^3 in Buffered zones. Slow-recovery zones also maintained higher pumping over the longer irrigation-season record, indicating that this difference was not limited to the 2012 drought. Precipitation varied across the MRVA but did not explain the recovery zones on its own (Supplementary Fig. S18).

The representative AEM sections and groundwater records show how these differences appeared at individual locations (Fig. 3a–c). Fast-recovery examples combined larger seasonal water-table fluctuations and repeated rebound with a thinner resistive interval. Slow-recovery examples occurred where thicker resistive, sand-rich deposits coincided with sustained pumping, whereas Buffered examples showed smaller water-table changes and more strongly layered subsurface structure. We further tested whether the mapped subsurface and pumping information could identify Slow-recovery locations without using the groundwater-response metrics that defined the zones. In 50-km spatial-block cross-validation, AEM resistivity alone gave a ROC-AUC of 0.787, compared with 0.579 for pumping alone, and combining AEM and pumping increased the ROC-AUC to 0.809 (Supplementary Fig. S20). The resulting probability map identified broad areas in the northern and central MRVA where the conditions associated with slow recovery were most common (Supplementary Fig. S15). Slow recovery was most strongly associated with the combination of thick, sand-rich aquifer structure

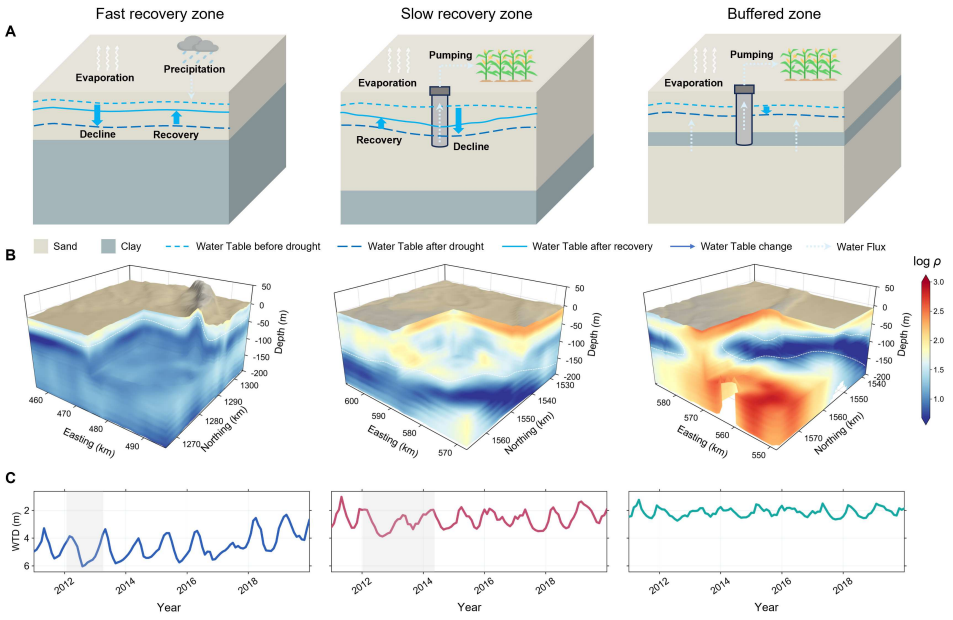

Fig. 3 Subsurface architecture and groundwater dynamics distinguish the three recovery zones. a, Conceptual hydrogeologic models of Fast-recovery, Slow-recovery and Buffered zones, illustrating differences in subsurface layering, pumping and water-table response during drought and recovery. **b**, Representative three-dimensional AEM resistivity sections from the three zones, shown in the same order as the conceptual models. **c**, Monthly WTD changes at the corresponding representative locations.

and intensive groundwater use. We next tested whether these same spatial differences also affected the groundwater response to reduced pumping.

Regional storage gain and local recovery favor different pumping allocations

The recovery zones identified above also differed in their response to reduced pumping. A separate diagnostic experiment, in which pumping was reduced by 20% in each management unit throughout 2012, showed strong spatial differences in local water-table recovery (Fig. 4a). Normalizing this response by the amount of pumping reduced gave a spatial measure of management leverage (Fig. 4b). Leverage was generally higher in Fast-recovery zones than in Slow-recovery and Buffered zones. We used

the 2012 leverage ranking to allocate pumping reductions during May–October 2013, while keeping the ranking fixed before the 2013 simulations. At the 20% conservation budget, 48.1% of the conserved pumping volume was allocated to Fast-recovery zones, 33.9% to Slow-recovery zones and 18.0% to Buffered zones (Fig. 4c).

Where pumping was reduced affected the regional groundwater response. During the 2012 drought, Leverage-guided allocation offset a larger fraction of the December storage deficit than Uniform or High-pumping allocation across the tested conservation budgets (Fig. 4d; Supplementary Fig. S24). At the common 20% budget, it offset 5.70% of the December 2012 deficit. The same 2012 leverage ranking remained useful during the following recovery period. With 3.299×10^9 m^3 of pumping conserved in 2013, Leverage-guided allocation produced 1.039×10^9 m^3 of storage benefit, compared with 0.919×10^9 m^3 under Uniform allocation and 0.769×10^9 m^3 under High-pumping allocation (Supplementary Fig. S23). The corresponding gains were 13.0% and 35.0%, showing that the location of pumping reductions affected how much groundwater was retained even when the total conserved volume was unchanged.

The larger regional storage gain did not lead to greater recovery everywhere. Before the May 2013 intervention, 19,649 cells had not yet reached half-recovery from the 2012 drought, and 76.52% of these cells were in Slow-recovery zones. By April 2014, Leverage-guided reductions advanced half-recovery in 3.19% of these initially unrecovered cells, compared with 3.77% under Uniform reductions at the same conserved volume (Supplementary Fig. S25). The difference was also present when recovery was measured continuously. Mean water-table improvement across initially unrecovered cells was 49.16 mm under Leverage-guided allocation and 54.95 mm under Uniform allocation, even though Leverage-guided allocation increased regional storage by 13.02% (Fig. 4g; Supplementary Fig. S27). The additional regional storage under Leverage-guided allocation came mainly from locations that had already recovered. Relative to Uniform allocation, initially unrecovered locations contributed $-19.90 \times$

10^6 m^3 to the storage difference, whereas already recovered locations contributed $+139.59 \times 10^6$ m^3, giving a net regional gain of 119.69×10^6 m^3 (Fig. 4e). Thus, the allocation that retained more groundwater across the MRVA did not provide greater recovery in the locations where drought deficits were still present.

The timing of pumping reductions also affected their benefit. For the same conserved volume and May–October intervention period, each cubic meter of pumping reduction produced 0.279 m^3 of storage benefit during the 2013 recovery period, compared with 0.225 m^3 during the 2012 drought, a 23.9% difference (Fig. 4f; Supplementary Fig. S26). Together, these experiments show that the amount of groundwater retained depended on both where and when pumping was reduced, while the allocation producing the larger regional storage gain did not provide greater recovery in the locations where drought deficits remained.

Discussion

Aquifer architecture and groundwater use organize post-drought recovery

Groundwater recovery after extreme drought varied markedly across the MRVA, and locations with the largest drought drawdown were not necessarily the slowest to recover. Groundwater responses can lag meteorological drought by months to years and vary strongly among aquifers and individual wells [12,15–17,44,45]. Groundwater decline and recovery can also occur within the same aquifer system, with some locations recovering as others remain depleted [14,20]. Our reconstruction resolves these contrasting responses within a single heavily pumped aquifer. Even after several wetter years, 40.6% of Slow-recovery locations still had mean water levels in 2019 below their 2011 mean, showing that groundwater recovery remained spatially uneven after the 2012 drought.

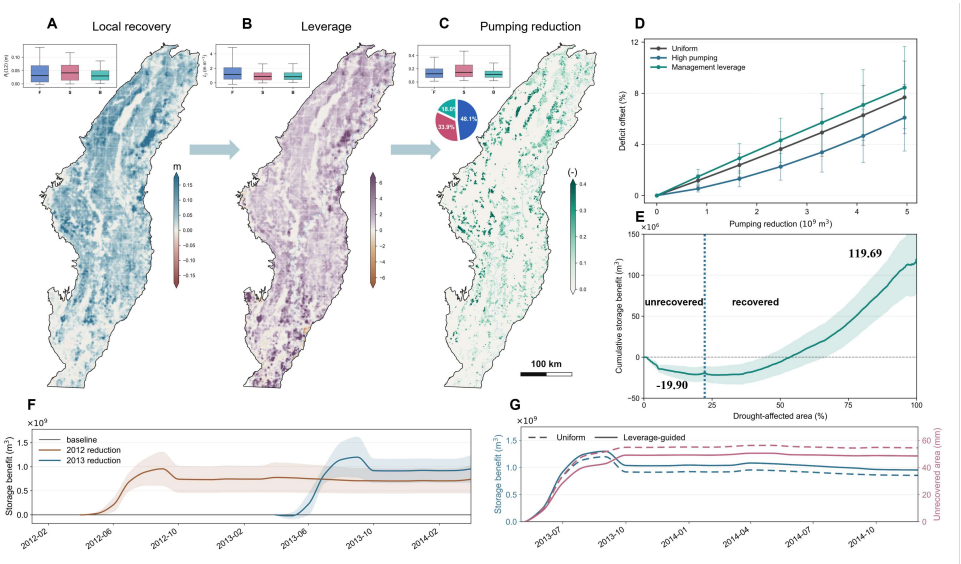

Fig. 4 Timing and spatial allocation shape groundwater benefits after extreme drought. **a**, Local recovery from separate 20% pumping reductions applied to each management unit throughout 2012; inset shows distributions across Fast-recovery, Slow-recovery and Buffered zones. **b**, Management leverage, defined as local recovery per unit pumping reduction, with corresponding zone distributions. **c**, Leverage-guided pumping reductions during May–October 2013 using the ranking derived from the 2012 diagnostic experiment; inset shows the allocation among recovery zones. **d**, Fraction of the December 2012 storage deficit offset by Uniform, High-pumping and Leverage-guided allocations as conserved pumping volume increases. **e**, Cumulative difference in storage benefit between Leverage-guided and Uniform allocations, ordered from locations unrecovered at the start of the 2013 intervention to those already recovered. **f**, Storage benefit through time for reductions applied during the 2012 drought and 2013 recovery period relative to historical pumping. **g**, Regional storage benefit and mean water-table improvement in initially unrecovered locations under Uniform and Leverage-guided allocations. Lines show model means; shading and error bars show variation among the five fitted models.

Slow recovery was concentrated where thick, resistive, sand-rich deposits coincided with intensive pumping. The lower Mississippi Valley contains strong spatial variation in alluvial architecture [23,24], with regional links between AEM resistivity and hydraulic properties [25] and intensive irrigation across productive parts of the MRVA [28–30,46]. The association with sand-rich structure does not mean that coarse aquifer material inherently recovers slowly. Thick permeable deposits provide productive groundwater resources, but they also support sustained withdrawals. The same properties that make groundwater readily available can therefore coincide with continued pumping pressure after meteorological drought has eased. This coupling between

aquifer architecture and groundwater use helps explain why Slow-recovery zones remained depleted despite subsequent wet years and supports our first hypothesis that post-drought recovery is organized by both subsurface structure and groundwater use.

Spatial allocation creates a trade-off between storage gain and local recovery

Groundwater recovery can be accelerated by changes in pumping, recharge and surface-water supply [18–21]. Global observations document cases in which long-term groundwater decline has reversed [20], and sustained human intervention together with favourable climate conditions has produced large-scale aquifer recovery in the North China Plain [21]. Our experiments address a related but different question: whether the same conserved pumping volume produces the same recovery when reductions are placed in different locations. Leverage-guided allocation increased regional storage by about 13% relative to Uniform allocation, yet initially unrecovered locations received less water-table improvement and fewer crossed the half-recovery threshold earlier. Management leverage identifies locations where a unit reduction in pumping produces a relatively large water-table response, but these locations need not be those with the largest remaining drought deficits. Regional storage also accumulates responses across area and specific yield, allowing already recovered locations to contribute strongly to the regional total. In our experiments, most of the additional storage under Leverage-guided allocation came from locations that had already recovered, whereas initially unrecovered locations contributed negatively to the difference. The places that retain the most additional groundwater and the places that most need recovery can therefore differ, supporting our second hypothesis that management outcomes depend on where pumping reductions are applied.

The timing of pumping reductions added another source of variation. The same conserved volume produced a larger storage benefit during the 2013 recovery period

than during the 2012 drought, although the two years differed in climate forcing and antecedent groundwater conditions. This does not imply that reductions should be postponed, because drought-period reductions still reduced the developing deficit. Differences in hydroclimatic conditions and management history can also alter groundwater recovery [14,19–21]. Our results add that benefits should also be evaluated after historical pumping resumes, because their persistence varies across the aquifer (Supplementary Figs. S21b and S22). Groundwater management also involves objectives beyond regional storage. Ecological targets depend on ecosystem response [47], while water availability, agricultural costs and other objectives can favor different management decisions [48–50]. Recent scenario work in the MRVA similarly emphasizes management at spatial scales relevant to pumping decisions [43]. Our 1-km grid may smooth groundwater variability at finer spatial scales. Additional local observations could help translate these regional patterns into site-specific pumping decisions. Our results support both hypotheses posed: post-drought recovery was organized by aquifer architecture and groundwater use, and these spatial differences also changed the response to reduced pumping. By shaping both recovery and the response to intervention, aquifer architecture links subsurface heterogeneity directly to groundwater-management outcomes. When pumping reductions are limited, their effects depend on the conserved volume and on where those reductions are applied. Regional storage gain and recovery of persistent deficits may favor different locations, making subsurface information relevant to how management actions are spatially targeted.

Methods

Airborne electromagnetic resistivity

Subsurface structure was derived from regional airborne electromagnetic (AEM) surveys over the Mississippi Alluvial Plain. In these surveys, controlled electromagnetic fields were transmitted from aircraft-mounted systems and the secondary fields induced in the subsurface were measured along flight lines [40,42]. After removal of noisy measurements associated with infrastructure and acquisition artefacts, the AEM responses were inverted as one-dimensional layered-earth models to estimate electrical resistivity beneath each flight path [40,42]. Frequency-domain Resolve data were inverted with Aarhus Workbench/AarhusInv, whereas time-domain Tempest data were inverted with GALEI, with sensor geometry, transmitter height, receiver offsets and attitude information included in the forward model where available [40,42]. The resulting along-line resistivity models were discretized to common 5-m depth intervals, interpolated by layer to the 1-km National Hydrogeologic Grid, and combined into a three-dimensional log10-resistivity product [42,51]. We sampled this gridded product at 70 depth levels from 0 to 350 m below land surface. Because electrical resistivity is sensitive to lithology, porosity, clay content and pore-water salinity, we treated it as a hydrostratigraphic proxy; higher resistivity was interpreted as more sand- or gravel-rich material where salinity effects are not dominant, and lower resistivity as finer-grained, less permeable material [40,52].

Graph neural-network reconstruction of monthly WTD

Monthly WTD was reconstructed on the 1-km MRVA grid with graph convolutional neural networks [53]. Each grid cell was represented as a graph node with static attributes describing AEM resistivity structure, topography and location-specific baseline conditions, and time-varying attributes describing monthly net infiltration, groundwater pumping and seasonality. Graph edges connected neighbouring cells,

with weights based on both horizontal proximity and similarity in AEM resistivity profile, so that message passing propagated information preferentially between cells that were close in space and hydrostratigraphically similar. The networks were implemented in PyTorch Geometric and trained to predict changes in water-table depth over 1-, 3- and 6-month intervals [54]. These horizon-specific predictions were recursively integrated between annual January anchor states from 2011 to 2023 and a December 2023 endpoint. The anchor states were derived from a spatially continuous long-term WTD reference [31], updated with shallow monitoring-well observations, so that the reconstruction retained both the regional spatial structure of the aquifer and the observed temporal evolution of water levels. The final monthly reconstruction was evaluated independently against CSR GRACE/GRACE-FO mascon liquid-water-equivalent anomalies [33,55].

Drought-response metrics and recovery-zone classification

We characterized groundwater response to the 2012 drought using five metrics calculated from reconstructed monthly WTD: maximum decline, decline rate, early recovery ratio, half-recovery time, and long-term recovery ratio. The pre-drought reference was defined as the shallowest WTD during January–April 2012, and the drought peak as the deepest WTD during May–October 2012. Early recovery was assessed during November 2012–April 2013, whereas long-term recovery was evaluated relative to mean WTD in 2011 and 2019. Grid cells were assigned to Fast-recovery, Slow-recovery, or Buffered zones according to their weighted Manhattan distance from predefined response prototypes in percentile-rank space.

Prediction of slow-recovery probability

We modelled groundwater drought vulnerability only after defining the response zones. We first assigned each grid cell to Fast recovery, Slow recovery or Buffered using drought-response metrics computed from the reconstructed water-table record. We

then withheld those response metrics and trained an ExtraTrees classifier to predict slow-recovery membership using only independently mapped predictors: the AEM resistivity profile, simple summary statistics of that profile, and groundwater pumping intensity [56,57]. Model performance was evaluated with five spatially blocked folds using 50-km blocks, reducing the risk that accuracy was inflated by spatial autocorrelation [58]. The final classifier produced a class-probability estimate, P_s, for each grid cell; we interpret high P_s as a Slow-recovery probability, meaning the probability that a location has the subsurface structure and pumping conditions associated with slow post-drought recovery.

Evaluation of pumping-reduction strategies

We evaluated groundwater responses to reduced pumping using the fitted GNN models while holding all other model inputs fixed. Seasonal pumping-reduction experiments were conducted from May through October in 2012 and 2013, with historical pumping restored after each intervention. Separately, a diagnostic experiment reduced pumping by 20% in each management unit individually throughout 2012 to quantify local recovery and derive management leverage. Management leverage was defined as the December 2012 water-table improvement divided by the equivalent depth of pumping reduction. The resulting 2012 leverage ranking was used to guide spatial allocation of pumping reductions. We compared Uniform, High-pumping and Leverage-guided allocations at the same total conserved pumping volume; the main comparison used a reduction equal to 20% of regional 2012 pumping. For the 2012 drought-period comparison, the leverage ranking was applied retrospectively, whereas the 2013 experiment used the 2012 ranking fixed before the intervention. Simulated water-table improvements were converted to regional storage benefit using the same spatially varying specific-yield field as in the groundwater reconstruction.

Statistical analyses

We estimated nominal 75% prediction intervals for reconstructed water-table depth using normalized split-conformal calibration on the temporal validation set. We evaluated the slow-recovery probability model using fivefold spatial cross-validation. The study area was divided into 50-km blocks, and all cells in a block were kept in the same fold. Each fold was withheld in turn. We calculated ROC-AUC, average precision and Brier score from the pooled out-of-fold predictions and also examined variation among folds. We ran each pumping-reduction scenario with five fitted graph neural-network models and reported the mean response. Unless otherwise stated, shaded bands and error bars show nominal central 75% between-model intervals calculated from the five-model mean and population standard deviation using the corresponding Gaussian quantile.

Data availability

All source datasets used in this study are publicly available from their original providers. The Mississippi Alluvial Plain boundary is available from the U.S. Geological Survey at https://doi.org/10.5066/F70R9NMJ [59]. Groundwater-level observations and site metadata are available through the U.S. Geological Survey Water Data for the Nation/National Water Information System at https://doi.org/10.5066/F7P55KJN [60] and through the U.S. Geological Survey Water Data APIs at https://api.waterdata.usgs.gov/ [61]. Airborne electromagnetic resistivity models and derivative hydrogeologic products for the Mississippi Alluvial Plain are available at https://doi.org/10.5066/P9382RCI [42]; the constituent airborne survey releases are listed in the Supplementary Information. Elevation data are available from the U.S. Geological Survey 3D Elevation Program [62]. Net-infiltration estimates are available from the U.S. Geological Survey Soil-Water-Balance data

release for 2000–2024 at https://doi.org/10.5066/P1YV4WD7 [63]. Groundwater-pumping estimates are available from AIWUM version 2.0 for 2014–2023 at https://doi.org/10.5066/P13PQXTH [64] and AIWUM version 1.1 for 2011–2013 at https://doi.org/10.5066/P9RGZOBZ [65]. Monthly precipitation data are available from Daymet version 4 Revision 1 at https://doi.org/10.3334/ORNLDAAC/2131 [66]. GRACE and GRACE-FO terrestrial-water-storage anomalies are available from the CSR RL06.3 Mascon Solutions v02 product at https://doi.org/10.15781/cgq9-nh24 [55]. River-network data are available from HydroRIVERS/HydroSHEDS [67]. The exact data versions and preprocessing procedures are described in the Supplementary Information.

The study-generated monthly WTD reconstruction is publicly available through Zenodo at https://doi.org/10.5281/zenodo.21695304 [68]. The archived NetCDF product contains monthly water-table depth and the nominal 75% prediction-interval radius for 87,871 active 1-km grid cells across the Mississippi River Valley alluvial aquifer from January 2011 through December 2023. It also contains projected and geographic coordinates, grid identifiers, and metadata indicating anchor months and direct groundwater observations. The exact versions of the source datasets and the preprocessing procedures used in this study are described in the Supplementary Information. A machine-readable inventory of the required input datasets and the checksum of the archived reconstruction product are provided in the associated code repository.

Code availability

The custom code and notebooks used to train the 1-, 3- and 6-month graph neural-network models, reconstruct monthly water-table depth, quantify reconstruction uncertainty, calculate drought-response metrics, assign groundwater-recovery zones, train and evaluate the Slow-recovery probability model, and perform the pumping-reduction, management-leverage, spatial-allocation and recovery analyses are publicly

available at https://github.com/ZhengyangFang/MRVA_WTD. The repository includes model configuration files, data-preprocessing and graph-construction code, model-training and reconstruction code, management-simulation modules, analysis notebooks, utility scripts, a machine-readable inventory of the required source datasets, and a locked Python environment. Large third-party datasets and intermediate model caches are not redistributed and must be obtained from their original providers. The repository will be versioned to preserve the exact code used for the published article.

Acknowledgements

We acknowledge the Integrated GroundWater Modeling Center (IGWMC) at Princeton University for providing access to HydroFrame resources and the high-resolution water-table-depth mapping code that we used in this study. We thank the U.S. Geological Survey for making groundwater-level observations, airborne electromagnetic survey data and derived hydrogeologic products, net-infiltration estimates from the Soil-Water-Balance model, AIWUM pumping estimates, and 3DEP elevation data publicly available. We also acknowledge the Oak Ridge National Laboratory Distributed Active Archive Center for the Daymet climate data, the Center for Space Research at the University of Texas at Austin for the CSR GRACE and GRACE-FO mascon products, and the HydroSHEDS team for the HydroRIVERS river-network data.

Funding

This work was supported by the University of Iowa Old Gold Summer Fellowship and startup fund from the University of Iowa.

Author contributions

Conceptualization: ZF, HC

Data curation: ZF, HC, YW

Formal analysis: ZF, ZL, HC

Funding acquisition: HC

Investigation: ZF, ZL, YW

Methodology: ZF, ZL, HC, DF, RG

Project administration: HC

Resources: HC

Software: ZF

Supervision: HC, RG, DF

Validation: ZF, HC

Visualization: ZF, YW

Writing – original draft: ZF, HC

Writing – review & editing: ZF, ZL, DF, YW, RG, HC

Competing interests

The authors declare no competing interests.

Supplementary information

Supplementary Information is available for this paper.

Correspondence and requests for materials

Correspondence and requests for materials should be addressed to Hang Chen (hchen117@uiowa.edu)

References

1. Van Loon, A. F. et al. Drought in the Anthropocene. Nat. Geosci. 9, 89–91 (2016). https://doi.org/10.1038/ngeo2646
2. Asoka, A., Gleeson, T., Wada, Y. & Mishra, V. Relative contribution of monsoon precipitation and pumping to changes in groundwater storage in India. Nat. Geosci. 10, 109–117 (2017). https://doi.org/10.1038/ngeo2869
3. Russo, T. A. & Lall, U. Depletion and response of deep groundwater to climate-induced pumping variability. Nat. Geosci. 10, 105–108 (2017). https://doi.org/10.1038/ngeo2883
4. Taylor, R. G. et al. Ground water and climate change. Nat. Clim. Change 3, 322–329 (2013). https://doi.org/10.1038/nclimate1744
5. Famiglietti, J. S. The global groundwater crisis. Nat. Clim. Change 4, 945–948 (2014). https://doi.org/10.1038/nclimate2425
6. Scanlon, B. R. et al. Groundwater depletion and sustainability of irrigation in the US High Plains and Central Valley. Proc. Natl Acad. Sci. USA 109, 9320–9325 (2012). https://doi.org/10.1073/pnas.1200311109
7. Gleeson, T., Wada, Y., Bierkens, M. F. P. & van Beek, L. P. H. Water balance of global aquifers revealed by groundwater footprint. Nature 488, 197–200 (2012). https://doi.org/10.1038/nature11295
8. MacDonald, A. M. et al. Groundwater quality and depletion in the Indo-Gangetic Basin mapped from in situ observations. Nat. Geosci. 9, 762–766 (2016). https://doi.org/10.1038/ngeo2791
9. Huang, Z. et al. Subregional-scale groundwater depletion detected by GRACE for both shallow and deep aquifers in North China Plain. Geophys. Res. Lett. 42, 1791–1799 (2015). https://doi.org/10.1002/2014GL062498

10. Getirana, A. et al. Deltaic freshwater scarcity driven by unsustainable groundwater-fed irrigation. Nat. Sustain. 8, 914–924 (2025). https://doi.org/10.1038/s41893-025-01566-0

11. de Graaf, I. E. M., Gleeson, T., van Beek, L. P. H., Sutanudjaja, E. H. & Bierkens, M. F. P. Environmental flow limits to global groundwater pumping. Nature 574, 90–94 (2019). https://doi.org/10.1038/s41586-019-1594-4

12. Hellwig, J., de Graaf, I. E. M., Weiler, M. & Stahl, K. Large-scale assessment of delayed groundwater responses to drought. Water Resour. Res. 56, e2019WR025441 (2020). https://doi.org/10.1029/2019WR025441

13. Peterson, T. J., Saft, M., Peel, M. C. & John, A. Watersheds may not recover from drought. Science 372, 745–749 (2021). https://doi.org/10.1126/science.abd5085

14. Alam, S. et al. Post-drought groundwater storage recovery in California's Central Valley. Water Resour. Res. 57, e2021WR030352 (2021). https://doi.org/10.1029/2021WR030352

15. Schreiner-McGraw, A. P. & Ajami, H. Delayed response of groundwater to multi-year meteorological droughts in the absence of anthropogenic management. J. Hydrol. 603, 126917 (2021). https://doi.org/10.1016/j.jhydrol.2021.126917

16. Bloomfield, J. P., Marchant, B. P., Bricker, S. H. & Morgan, R. B. Regional analysis of groundwater droughts using hydrograph classification. Hydrol. Earth Syst. Sci. 19, 4327–4344 (2015). https://doi.org/10.5194/hess-19-4327-2015

17. Cuthbert, M. O. et al. Observed controls on resilience of groundwater to climate variability in sub-Saharan Africa. Nature 572, 230–234 (2019). https://doi.org/10.1038/s41586-019-1441-7

18. Orduña Alegría, M. E. et al. Unlocking aquifer sustainability through irrigator-driven groundwater conservation. Nat. Sustain. 7, 1574–1583 (2024). https://doi.org/10.1038/s41893-024-01437-0

19. Sharma, C. et al. Efficacy of mitigation strategies for aquifer sustainability under climate change. Nat. Sustain. 8, 44–53 (2025). https://doi.org/10.1038/s41893-024-01477-6

20. Jasechko, S. et al. Rapid groundwater decline and some cases of recovery in aquifers globally. Nature 625, 715–721 (2024). https://doi.org/10.1038/s41586-023-06879-8

21. Long, D. et al. Unprecedented large-scale aquifer recovery through human intervention. Nat. Commun. 16, 7296 (2025). https://doi.org/10.1038/s41467-025-62719-5

22. Aeschbach-Hertig, W. & Gleeson, T. Regional strategies for the accelerating global problem of groundwater depletion. Nat. Geosci. 5, 853–861 (2012). https://doi.org/10.1038/ngeo1617

23. Minsley, B. J. et al. Airborne geophysical surveys of the lower Mississippi Valley demonstrate system-scale mapping of subsurface architecture. Commun. Earth Environ. 2, 131 (2021). https://doi.org/10.1038/s43247-021-00200-z

24. Song, Y., Tsai, F. T.-C., Minsley, B. J., Wu, C. & Heggy, E. Quantitative subsurface characterization illuminates the origin of the Quaternary Mississippi River Valley alluvial aquifer. Commun. Earth Environ. 6, 646 (2025). https://doi.org/10.1038/s43247-025-02545-1

25. Ikard, S. J., Minsley, B. J., Rigby, J. R. & Kress, W. H. A model of transmissivity and hydraulic conductivity from electrical resistivity distribution derived from airborne electromagnetic surveys of the Mississippi River Valley Alluvial Aquifer, Midwest USA. Hydrogeol. J. 31, 313–334 (2023). https://doi.org/10.1007/s10040-022-02590-6

26. Alley, W. M., Healy, R. W., LaBaugh, J. W. & Reilly, T. E. Flow and storage in groundwater systems. Science 296, 1985–1990 (2002). https://doi.org/10.1126/science.1067123

548 27. Condon, L. E. & Maxwell, R. M. Simulating the sensitivity of evapotranspiration
549 and streamflow to large-scale groundwater depletion. Sci. Adv. 5, eaav4574 (2019).
550 https://doi.org/10.1126/sciadv.aav4574
551 28. Clark, B. R., Hart, R. M. & Gurdak, J. J. Groundwater availability of the Missis-
552 sippi embayment. U.S. Geological Survey Professional Paper 1785 (U.S. Geological
553 Survey, 2011). https://doi.org/10.3133/pp1785
554 29. Leaf, A. T., Duncan, L. L., Haugh, C. J., Hunt, R. J. & Rigby, J. R. Simulating
555 groundwater flow in the Mississippi Alluvial Plain with a focus on the Missis-
556 sippi Delta. U.S. Geological Survey Scientific Investigations Report 2023–5100 (U.S.
557 Geological Survey, 2023). https://doi.org/10.3133/sir20235100
558 30. Majumdar, S. et al. Improving crop-specific groundwater use estimation in the
559 Mississippi Alluvial Plain: implications for integrated remote sensing and machine
560 learning approaches in data-scarce regions. J. Hydrol. Reg. Stud. 52, 101674 (2024).
561 https://doi.org/10.1016/j.ejrh.2024.101674
562 31. Ma, Y. et al. High resolution US water table depth estimates reveal quantity of
563 accessible groundwater. Commun. Earth Environ. 7, 45 (2026). https://doi.org/10
564 .1038/s43247-025-03094-3
565 32. Rodell, M. et al. Estimating groundwater storage changes in the Mississippi River
566 basin (USA) using GRACE. Hydrogeol. J. 15, 159–166 (2007). https://doi.org/10
567 .1007/s10040-006-0103-7
568 33. Tapley, B. D., Bettadpur, S., Watkins, M. & Reigber, C. The gravity recovery and
569 climate experiment: mission overview and early results. Geophys. Res. Lett. 31,
570 L09607 (2004). https://doi.org/10.1029/2004GL019920
571 34. Binley, A. et al. The emergence of hydrogeophysics for improved understanding of
572 subsurface processes over multiple scales. Water Resour. Res. 51, 3837–3866 (2015).
573 https://doi.org/10.1002/2015WR017016

574 35. Barfod, A. A. S., Møller, I. & Christiansen, A. V. Compiling a national resistivity
575 atlas of Denmark based on airborne and ground-based transient electromagnetic
576 data. J. Appl. Geophys. 134, 199–209 (2016). https://doi.org/10.1016/j.jappgeo.20
577 16.09.017
578 36. Delsman, J. R. et al. Large-scale, probabilistic salinity mapping using airborne elec-
579 tromagnetics for groundwater management in Zeeland, the Netherlands. Environ.
580 Res. Lett. 13, 084011 (2018). https://doi.org/10.1088/1748-9326/aad19e
581 37. Knight, R. et al. Mapping aquifer systems with airborne electromagnetics in the
582 Central Valley of California. Groundwater 56, 893–908 (2018). https://doi.org/10
583 .1111/gwat.12656
584 38. Kang, S., Knight, R. & Goebel, M. Improved imaging of the large-scale structure
585 of a groundwater system with airborne electromagnetic data. Water Resour. Res.
586 58, e2021WR031439 (2022). https://doi.org/10.1029/2021WR031439
587 39. Knight, R. et al. Airborne geophysical method images fast paths for managed
588 recharge of California's groundwater. Environ. Res. Lett. 17, 124021 (2022). https:
589 //doi.org/10.1088/1748-9326/aca344
590 40. Siemon, B., Christiansen, A. V. & Auken, E. A review of helicopter-borne electro-
591 magnetic methods for groundwater exploration. Near Surf. Geophys. 7, 629–646
592 (2009). https://doi.org/10.3997/1873-0604.2009043
593 41. Minsley, B. J. et al. The saline groundwater legacy of a large buried coastal paleo-
594 estuary. Nat. Commun. 17, 9119 (2026). https://doi.org/10.1038/s41467-026-760
595 05-5
596 42. James, S. R. & Minsley, B. J. Combined results and derivative products of hydro-
597 geologic structure and properties from airborne electromagnetic surveys in the
598 Mississippi Alluvial Plain (ver. 2.0, July 2024). U.S. Geological Survey data release
599 (2021). https://doi.org/10.5066/P9382RCI

43. Traylor, J. P. et al. Scenarios to assess the future water availability in the Mississippi River Valley Alluvial Aquifer for the Cache River and Grand Prairie Regions of Arkansas. ESS Open Archive (2026). https://doi.org/10.22541/essoar.15004472/v1

44. Mao, S., Ellsworth, W. L., Zheng, Y. & Beroza, G. C. Depth-dependent seismic sensing of groundwater recovery from the atmospheric-river storms of 2023. Science 387, 758–763 (2025). https://doi.org/10.1126/science.adr6139

45. Cuthbert, M. O. et al. Global patterns and dynamics of climate–groundwater interactions. Nat. Clim. Change 9, 137–141 (2019). https://doi.org/10.1038/s41558-018-0386-4

46. Lovelace, J. K., Nielsen, M. G., Read, A. L., Murphy, C. J. & Maupin, M. A. Estimated groundwater withdrawals from principal aquifers in the United States, 2015. U.S. Geological Survey Circular 1464 (U.S. Geological Survey, 2020). https://doi.org/10.3133/cir1464

47. Rohde, M. M. et al. Establishing ecological thresholds and targets for groundwater management. Nat. Water 2, 312–323 (2024). https://doi.org/10.1038/s44221-024-00221-w

48. Perez, N. et al. Ending groundwater overdraft without affecting food security. Nat. Sustain. 7, 1007–1017 (2024). https://doi.org/10.1038/s41893-024-01376-w

49. Jaeger, W. K., Antle, J., Gingerich, S. B. & Bigelow, D. Advancing sustainable groundwater management with a hydro-economic system model: Investigations in the Harney Basin, Oregon. Water Resour. Res. 60, e2023WR036972 (2024). https://doi.org/10.1029/2023WR036972

50. Markovich, K. H. et al. Multi-objective optimization of a hydro-economic model in an over-allocated agricultural basin. Groundwater 64, 278–294 (2026). https://doi.org/10.1111/gwat.70051

51. Clark, B. R. et al. National-scale grid to support regional groundwater availability studies and a national hydrogeologic framework. U.S. Geological Survey data release (2018). https://doi.org/10.5066/F7P84B24

52. Palacky, G. J. Resistivity characteristics of geologic targets. In Electromagnetic Methods in Applied Geophysics, Vol. 1 (ed. Nabighian, M. N.) chap. 3 (Society of Exploration Geophysicists, 1988). https://doi.org/10.1190/1.9781560802631.ch3

53. Kipf, T. N. & Welling, M. Semi-supervised classification with graph convolutional networks. In Proceedings of the 5th International Conference on Learning Representations (2017).

54. Fey, M. & Lenssen, J. E. Fast graph representation learning with PyTorch Geometric. ICLR Workshop on Representation Learning on Graphs and Manifolds (2019). https://doi.org/10.48550/arXiv.1903.02428

55. Save, H. CSR GRACE and GRACE-FO RL06 Mascon Solutions v02. Center for Space Research, University of Texas at Austin (2020). https://doi.org/10.15781/cgq9-nh24

56. Geurts, P., Ernst, D. & Wehenkel, L. Extremely randomized trees. Mach. Learn. 63, 3–42 (2006). https://doi.org/10.1007/s10994-006-6226-1

57. Pedregosa, F. et al. Scikit-learn: machine learning in Python. J. Mach. Learn. Res. 12, 2825–2830 (2011). https://jmlr.org/papers/v12/pedregosa11a.html

58. Roberts, D. R. et al. Cross-validation strategies for data with temporal, spatial, hierarchical, or phylogenetic structure. Ecography 40, 913–929 (2017). https://doi.org/10.1111/ecog.02881

59. Painter, J. A. & Westerman, D. A. Mississippi Alluvial Plain Extent, November 2017. U.S. Geological Survey data release (2018). https://doi.org/10.5066/F70R9NMJ

60. U.S. Geological Survey. USGS Water Data for the Nation: U.S. Geological Survey National Water Information System database. https://doi.org/10.5066/F7P55KJN (accessed 29 April 2026)
61. U.S. Geological Survey. USGS Water Data APIs. https://api.waterdata.usgs.gov/ (accessed 20 October 2026)
62. U.S. Geological Survey. 1/3rd arc-second Digital Elevation Models (DEMs) - USGS National Map 3DEP Downloadable Data Collection. U.S. Geological Survey data release. https://data.usgs.gov/datacatalog/data/USGS:3a81321b-c153-416f-98b7-cc8e5f0e17c3 (accessed 29 April 2026)
63. Villers, J. J., Haugh, C. M. & Duncan, L. L. Updated Estimates of Water Budget Components for the Mississippi Embayment Region Using a Soil-Water-Balance Model, 2000–2024. U.S. Geological Survey data release (2026). https://doi.org/10.5066/P1YV4WD7.
64. Haugh, C. M. Aquaculture and Irrigation Water-Use Model (AIWUM) version 2.0 updated input and output datasets for the Mississippi Alluvial Plain, 2014–2023. U.S. Geological Survey data release (2026). https://doi.org/10.5066/P13PQXTH
65. Bristow, E. L. & Wilson, J. L. Aquaculture and irrigation water-use model (AIWUM) version 1.1 estimates and related datasets for the Mississippi Alluvial Plain. U.S. Geological Survey data release (2023). https://doi.org/10.5066/P9RGZOBZ
66. Thornton, M. M., Shrestha, R., Wei, Y., Thornton, P. E. & Kao, S.-C. Daymet: Monthly Climate Summaries on a 1-km Grid for North America, Version 4 R1. ORNL DAAC (2022). https://doi.org/10.3334/ORNLDAAC/2131.
67. Lehner, B. & Grill, G. Global river hydrography and network routing: baseline data and new approaches to study the world's large river systems. Hydrol. Process. 27, 2171–2186 (2013). https://doi.org/10.1002/hyp.9740

68. Fang, Z. Monthly 1-km water-table depth reconstruction for the Mississippi River Valley alluvial aquifer from 2011 to 2023. Zenodo, version 1.0.0 (2026). https://doi.org/10.5281/zenodo.21695304

Supplementary Files

This is a list of supplementary files associated with this preprint. Click to download.

- supplementary.pdf